Energy & Environmental Science

ROYAL SOCIETY OF CHEMISTRY

PAPER

View Article Online
View Journal | View Issue

Cite this: *Energy Environ. Sci.*, 2020, **13**, 1832

Unveiling the mechanisms of lithium dendrite suppression by cationic polymer film induced solid–electrolyte interphase modification†

Seung-Yong Lee,[a] Junyi Shangguan,[ab] Judith Alvarado,[c] Sophia Betzler,[a] Stephen J. Harris,[a] Marca M. Doeff[c] and Haimei Zheng*[ab]

Received 17th February 2020,
Accepted 1st May 2020

DOI: 10.1039/d0ee00518e

rsc.li/ees

It is crucial to suppress lithium dendrite formation in lithium metal batteries. Formation of a good solid–electrolyte interphase (SEI) has been considered to be effective in limiting lithium dendrite growth. However, how the SEI may be modified during lithium deposition is hard to resolve due to challenges in *in situ* investigation of the SEI with fine details. We report an *in situ* study that uncovers the lithium dendrite suppression mechanism arising from SEI modification by a poly(diallyldimethylammonium chloride) (PDDA) cationic polymer film, using electrochemical liquid cell transmission electron microscopy (TEM). Lithium nanogranules are obtained in the presence of the polymer film. Chemical mapping of the deposits provides remarkable details of the SEI on individual nanogranules. It shows that lithium fluorides are uniformly distributed within the inner SEI layer of individual lithium nanogranules, arising from the instantaneous reaction of the deposited lithium with PF_6^- ions accumulated by the cationic polymer film, and thus the dendritic growth of lithium is prohibited. The ability to directly measure SEI chemistry at the nanoscale down to the individual nanograins *in situ* and unveil its correlation with the lithium deposition behavior opens future opportunities to explore unsolved mechanisms in batteries.

Broader context

Dendritic growth of lithium metal is a primary concern for the development of high energy lithium metal batteries. It is known that the solid–electrolyte interphase (SEI) plays a vital role in controlling the lithium growth. There have been reports that a polymer film coating on the lithium metal anode can improve the battery performance, likely resulting from the modification of the SEI. However, how the SEI is modified at the nanoscale and thus suppresses the lithium dendrite formation is unclear. This is due to challenges in directly characterizing the SEI, since the SEI is sensitive to air exposure and may be damaged by post processing. Here, through *in situ* liquid cell transmission electron microscopy with nanoscale chemical imaging of the SEI, our study revealed the mechanisms of lithium dendrite suppression induced by a poly(diallyldimethylammonium chloride) (PDDA) cationic polymer film. We found that the rapid formation of a 50–100 nm-thick LiF-rich SEI layer leads to the growth of lithium nanogranules. This work suggests a unique approach to obtain a LiF-rich SEI without supplying extra fluorine in the electrolyte. The capability of *in situ* nanoscale chemical imaging of the SEI provides opportunities to explore the fundamental mechanisms behind the performance of batteries.

Introduction

Lithium metal anodes have a more than ten times higher theoretical specific capacity than graphite anodes currently used in lithium ion batteries. However, dendritic growth of lithium metal results in shortened cycle life of devices utilizing these anodes and can cause serious safety issues. Thus, the exploration of effective means to limit the lithium dendrite formation is significant for developing next generation high energy batteries.[1] Many studies have shown that polymer films coated on the lithium anode can successfully suppress the growth of lithium dendrites.[2] For instance, improved performance has been achieved in lithium metal batteries with polymer film coated electrodes.[3–8] The suppression of dendrite growth is often attributed to the mechanical properties of the polymer films[3–5] or the improved physicochemical properties of the solid–electrolyte interphase (SEI) formed on lithium metal by

[a] *Materials Sciences Division, Lawrence Berkeley National Laboratory, Berkeley, CA, USA. E-mail: hmzheng@lbl.gov*
[b] *Department of Material Science and Engineering, University of California, Berkeley, CA, USA*
[c] *Energy Storage and Distributed Resources Division, Lawrence Berkeley National Laboratory, Berkeley, CA, USA*

† Electronic supplementary information (ESI) available: Supplementary notes, supplementary figures and tables, and *in situ* TEM videos. See DOI: 10.1039/d0ee00518e

electrolyte decomposition.[6–8] It is well known that the SEI plays a critical role in allowing the lithium anode to function in batteries.[1] However, since the SEI and lithium metal are sensitive to air exposure and may be damaged by post processing, it has been a great challenge to directly study the SEI on lithium experimentally.[9] So far, it is unclear how the SEI is modified (*e.g.*, by a polymer film) at the nanoscale and thus suppresses lithium dendrite formation.

A variety of methods[10–15] have been used to investigate the SEI including spectroscopic techniques such as X-ray photoelectron spectroscopy (XPS), Fourier-transform infrared (FTIR) spectroscopy, Raman spectroscopy, *etc.* Characterizations with spectroscopic methods have contributed to the understanding of SEI chemistry.[9,15] However, due to the limited spatial resolution, it is hard to resolve the structure and chemistry of the SEI at the nanoscale.[10–12] In contrast, transmission electron microscopy (TEM) is powerful in providing spatially resolved information. For example, TEM operated at cryogenic temperatures (Cryo-EM) has recently been used to study the SEI and an unprecedented level of information on the structures of the SEI has been achieved.[13,14] However, damage to the SEI during post processing of the sample is a major concern. In order to reveal the modifications of SEI fine structure induced changes in the growth behavior of lithium, *in situ* TEM studies of the dynamic electrochemical deposition of lithium can be the most effective approach.

We investigate the mechanisms of lithium dendrite suppression by a poly(diallyldimethylammonium chloride) (PDDA) cationic polymer film through direct measurement of the SEI using *in situ* electrochemical liquid cell TEM. PDDA is an attractive high charge density cationic polyelectrolyte,[16–18] which is multifunctional in battery applications including as a polymer electrolyte.[18–23] The PDDA polymer electrolyte has shown high Li-ion conductivity, and chemical and thermal stabilities.[17] It has been reported that a PDDA film on the anode can improve the performance of lithium metal batteries,[17,19] however the underlying mechanisms are still unsolved. We consider that the beneficial results are unlikely derived from the mechanical suppression of lithium dendrites by the polymer film itself, since the PDDA film may not offer better mechanical properties than a typical separator.[24–27] In this work, we directly compare the dynamic electrochemical deposition of lithium in liquid TEM cells and characterize their SEIs under conditions with and without the PDDA cationic polymer film. Changes in the lithium growth behavior due to the polymer density variations are also studied. Importantly, direct mapping of the chemical distribution within the SEI is accomplished using scanning TEM (STEM) energy-dispersive X-ray spectroscopy (EDS) without using destructive techniques or low temperature experiments.[13,14] Our *in situ* experiment results are also supported by coin cell battery experiments, which validate the nanoscale *in situ* approach.[28] This study allows us to unveil the mechanisms of lithium dendrite suppression by a polymer film through modifications of the SEI chemistry. It demonstrates significant advances in the investigation of spatially resolved SEI chemistry with *in situ* experiments. The results expand our knowledge on lithium dendrite suppression and controlling lithium SEI chemistry, which is essential for future lithium battery development.

Results and discussion

In situ lithium growth under a cationic polymer film

A schematic design of the *in situ* electrochemical liquid cell TEM setup is shown in Fig. 1a. A Li/Li symmetric cell is constructed by attaching lithium flakes onto Ti electrodes and using 1 M $LiPF_6$ in propylene carbonate (PC) as the electrolyte. The top and bottom Si/SiN chips are sealed using an ultraviolet-curing adhesive, which is much more effective in trapping liquid electrolytes in the electrochemical liquid TEM cell than some previously reported methods.[29,30] A sweep–step function (linear sweep potential followed by constant potential bias at the ending potential) is applied to the device for *in situ* lithium plating in the electrochemical liquid TEM cell. The reaction dynamics are recorded using a charge-coupled device (CCD) at two frames per second. Details of the design and fabrication of the electrochemical liquid TEM cell are elaborated in the Experimental section.

It is challenging to coat the PDDA film in the thin electrochemical liquid TEM cell with controlled polymer density (the chemical structure of PDDA is shown in Fig. 1a). Here we introduce a unique method. By taking advantage of the fact that PDDA is also widely used as a surfactant in colloidal nanocrystal synthesis,[31,32] we prepare a dilute solution of PDDA with $Sn@SnO_2$ nanostructures (Sn nanowires/nanoparticles with a thin layer of surface oxide). The PDDA chains adhere to the surface of the $Sn@SnO_2$ nanostructures by electrostatic attraction, while some remain free in the solvent (see details in the ESI† and Fig. S1). The solution is loaded through a reservoir of the electrochemical liquid cell and is drawn into the cell by capillary force (Fig. S2, ESI†). After the solvent has evaporated, the electrodes of the electrochemical liquid cell are coated with the PDDA polymer film (see a schematic drawing in Fig. 1b and optical microscope images in Fig. S3, ESI†). The cationic polymer area density can be controlled by varying the area density of $Sn@SnO_2$ nanostructures on the electrodes. It is known that Sn and SnO_2 experience large volume changes when they react with lithium ions in lithium-ion batteries.[33] Here, the $Sn@SnO_2$ nanostructures remain inert without participating in reactions during lithium deposition (Fig. S4, ESI†). This is likely due to their high contact resistance with the electrodes in the cell. According to previous studies,[34,35] heating or welding is necessary in order to make sufficient electrical contact between the nanoparticles and electrodes in electrochemical liquid TEM cells. The effectiveness of the $Sn@SnO_2$ nanostructure-assisted PDDA coating method is further discussed in the ESI.†

A representative *in situ* lithium electrodeposition by liquid cell TEM in the presence of the $Sn@SnO_2$ nanostructure-assisted cationic polymer film is shown in Fig. 1c (also see Video S1, ESI†). After the application of the linear sweep potential, the lithium

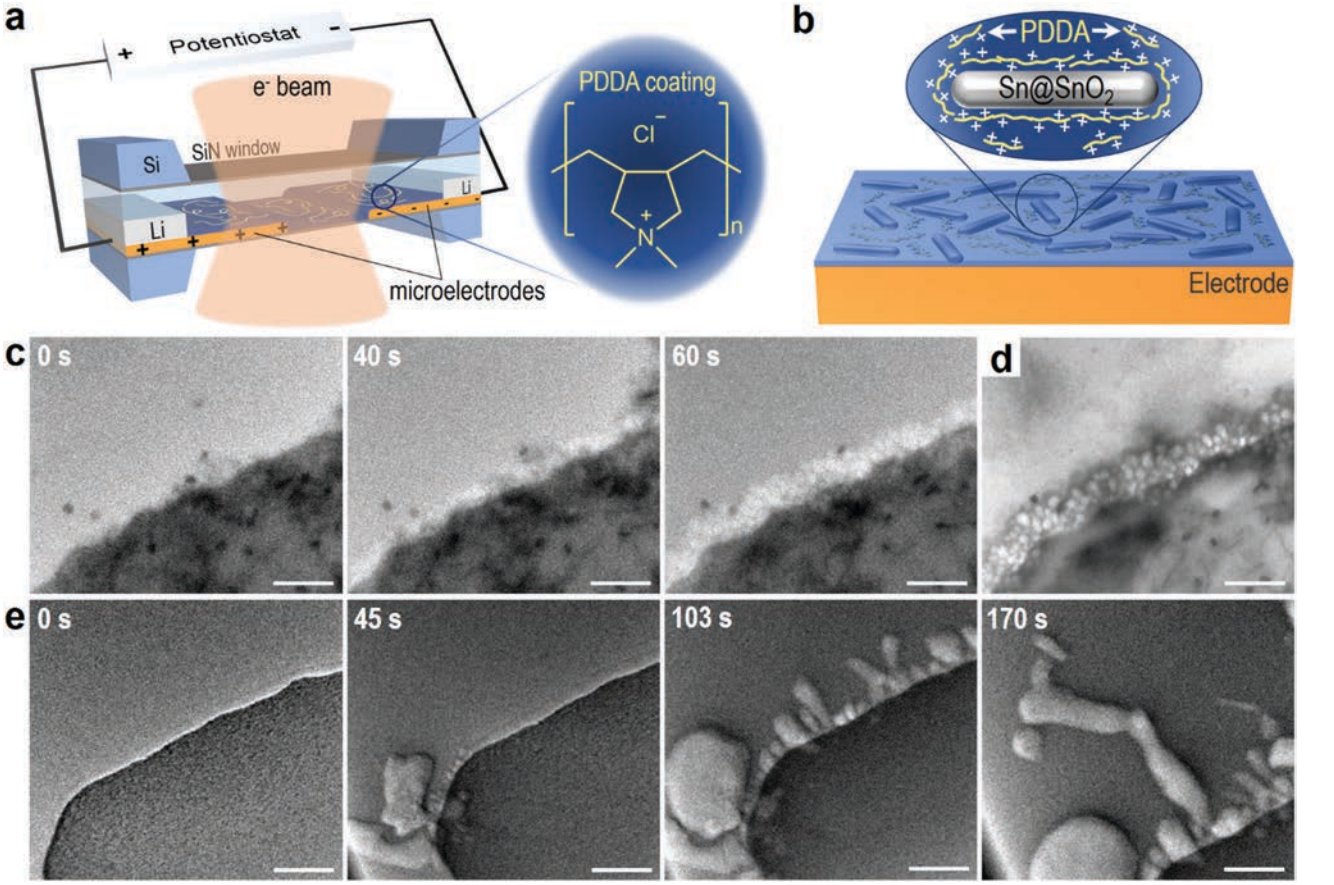

Fig. 1 *In situ* electrochemical liquid cell transmission electron microscopy (TEM) investigation of the cationic polymer film effects on the electrochemical deposition of lithium. (a) A schematic design of the *in situ* liquid cell TEM experiment with a cationic polymer coating. The chemical structure of the cationic polymer, poly(diallyldimethylammonium chloride) (PDDA), is also shown. (b) A schematic drawing of $Sn@SnO_2$ nanostructure-assisted cationic polymer coating for the *in situ* liquid TEM experiment. (c) Sequential TEM images of *in situ* lithium metal plating in the presence of the $Sn@SnO_2$ nanostructure-assisted cationic polymer coating layer (Video S1, ESI†). (d) A TEM image obtained after the *in situ* liquid cell TEM experiment corresponding to (c). (e) Sequential TEM images of *in situ* lithium dendritic growth in an electrochemical liquid cell without the polymer film (Video S3, ESI†). All scale bars are 1 μm.

begins to deposit at the edge of the electrode, where a higher electric field is expected. The bright contrast of lithium is attributed to the lower scattering cross-section of electrons in lithium metal than in Ti, Sn, or lithium compounds. Lithium nanogranules with an average size of 200 nm are plated on the electrode without any protruding dendrites (Fig. 1d). More results on lithium nanogranular growth with the cationic polymer coating can be found in Fig. S5 (ESI†). As control experiments, the growth of lithium nanogranules without electron beam irradiation (Fig. S6, ESI†) or without the assistance of $Sn@SnO_2$ nanostructures is also demonstrated (Fig. S7 and Video S2, ESI†). Further details of the control experiments are provided in the ESI.†

We compare *in situ* lithium plating without the polymer film to these results. Similar to what has been observed in previous studies,[36,37] lithium is irregularly plated on the electrode, which promotes dendritic growth (Fig. 1e and Video S3, ESI†). As shown in Fig. 1e, the morphology of individual dendritic grains varies, likely due to the nanoscale inhomogeneity of the local environments.[38] The trajectory of lithium volume changes and the estimated current densities with time show similar trends in both cases, with and without the cationic polymer coating, as shown in Fig. 2. This shows that the cationic polymer film changes the lithium growth behavior and morphology.

We investigate the nucleation and growth dynamics of individual lithium nanogranules to understand the mechanisms of their growth in the presence of the cationic polymer film. Sequential TEM images show the growth of several lithium nanogranules (Fig. 3a and Video S4, ESI†). It is hard to distinguish the SEI at the initial state (at 0 s) due to the low contrast and limited spatial resolution under the imaging conditions (*e.g.*, thick liquid cells, low dose imaging, *etc.*). However, dark regions can be identified on the electrode after a potential has been applied for 11–17 seconds. Since the subsequent lithium deposition appears to be brighter and the dimensions of dark regions are consistent with the lithium nanogranules, we consider the dark regions to correspond to the SEI on lithium. Interestingly, the deposition of thick SEI layers (more than 100 nm) is observed as soon as lithium is deposited (Fig. 3a), or even before lithium growth can be clearly identified (Fig. S9a, ESI†). This implies that reactions with the electrolyte occur instantaneously when lithium is

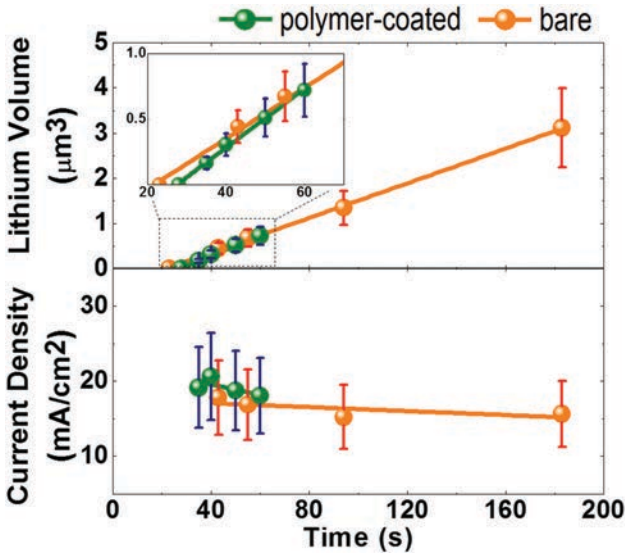

Fig. 2 Lithium volume changes and current density profiles as a function of time (calculated based on the *in situ* TEM Videos S1 and S3, ESI†). Measurement errors are indicated on the plot. Linear regression lines are also drawn on the plot.

deposited, which leads to the rapid formation of the SEI. This behavior can also be recognized in a plot of how the lithium nanogranule size changes with time (Fig. 3b and Fig. S9b, ESI†). In addition to the fast development of the SEI at the early stages, another distinct feature is that the lithium nanogranules stop growing after they reach critical sizes (about 150–450 nm). In the meantime, the SEI becomes darker, suggesting that its density has increased. Our observations suggest that the chemistry of the SEI likely plays a major role in lithium nanogranular growth and the inhibition of dendrite formation, as discussed later in the manuscript.

We next examine the final sizes and stability of lithium nanogranules grown under different densities of the cationic polymer coating (Fig. 3c). Since the ratio of PDDA to $Sn@SnO_2$ nanostructures in the solution is fixed, the area density of the polymer coating can be estimated by that of $Sn@SnO_2$ nanostructures in the film (see detailed measurements in the ESI† and Table S1). The size distributions of the lithium nanogranules are obtained from a set of *in situ* TEM experiments where the cationic polymer density varies (Fig. S10 and Table S1; see the ESI† for more details on the discussions of the nanogranule size measurements). The results show distinct trends. First, higher cationic polymer densities result in smaller lithium

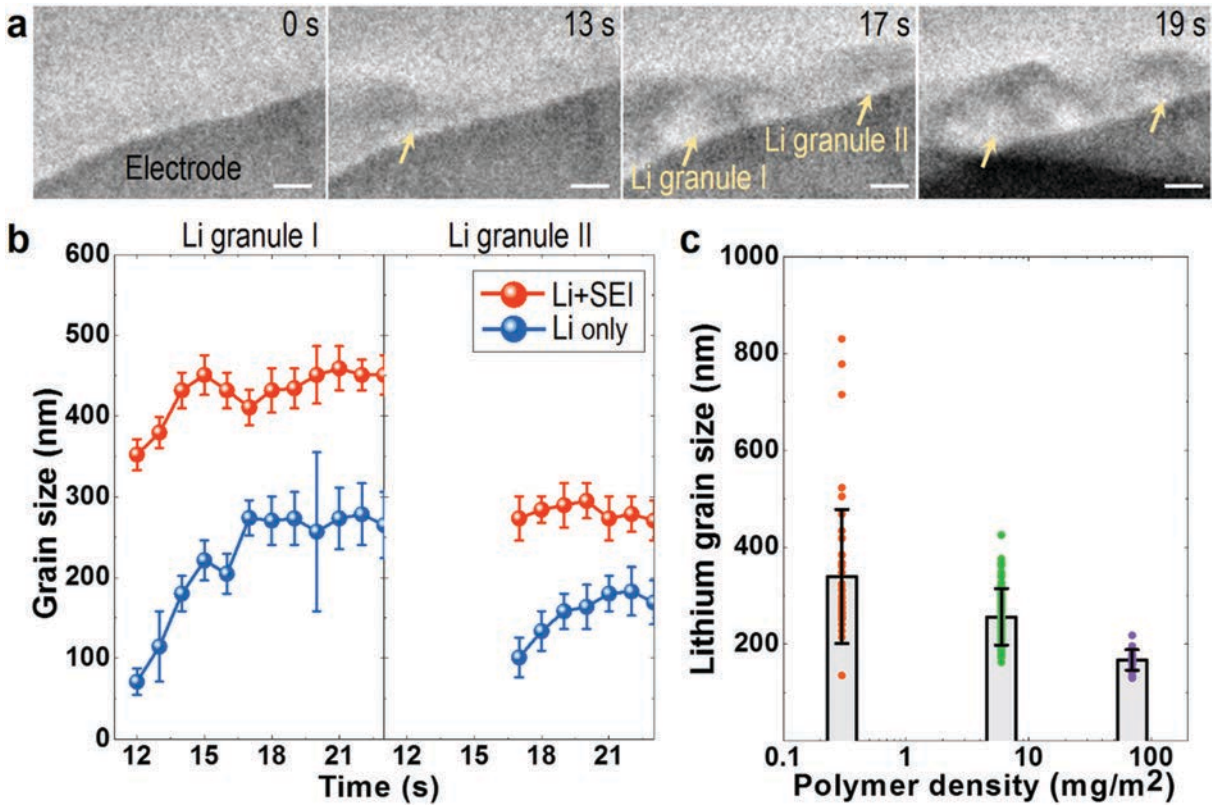

Fig. 3 *In situ* observations of lithium nanogranular growth in the presence of the PDDA cationic polymer coating. (a) Sequential TEM images showing the growth behaviors of lithium and solid-electrolyte interphase (SEI) layers. Scale bars are 200 nm. (b) Size evolution of representative lithium nanogranules during lithium deposition. Measurement errors are indicated. Details of the measurement are shown in Fig. S8 (ESI†). (c) Size distribution of lithium nanogranules as a function of the cationic polymer area density. Data were obtained from a set of *in situ* TEM experiments where the cationic polymer area density varies. The diameter of each lithium nanogranule is shown as solid dots. Columns and error bars indicate the average diameter and the standard deviation of lithium nanogranules in each sample.

nanogranules. Second, the size distribution of nanogranules becomes narrower as the cationic polymer density increases. In the case of a very low density of cationic polymer (*e.g.*, Case I in Fig. S10, ESI,† with an estimated polymer density of 0.3 mg m^{-2}), there is a large size distribution of lithium nanogranules, suggesting that the lithium nanogranules become unstable and are prone to form dendrites.

Chemical imaging of the SEI on lithium nanogranules

We further analyze the SEI on lithium nanogranules non-destructively using STEM-EDS by taking full advantage of the *in situ* TEM experiments. The lithium nanogranules grown in a liquid TEM cell from the *in situ* experiments are characterized without being exposed to air (see more detailed sample preparation in the Experimental section and ESI†). A representative high-angle annular dark field (HAADF) STEM image shows many dark round lithium nanogranules in the field of view (Fig. 4a). Lithium appears dark in the HAADF STEM image because of its low atomic mass featuring low scattering angles. We focus on chemical mapping of the distribution of carbon (C), oxygen (O), fluorine (F), and phosphorus (P) within the SEI layer relative to their distribution in the electrolyte residue in

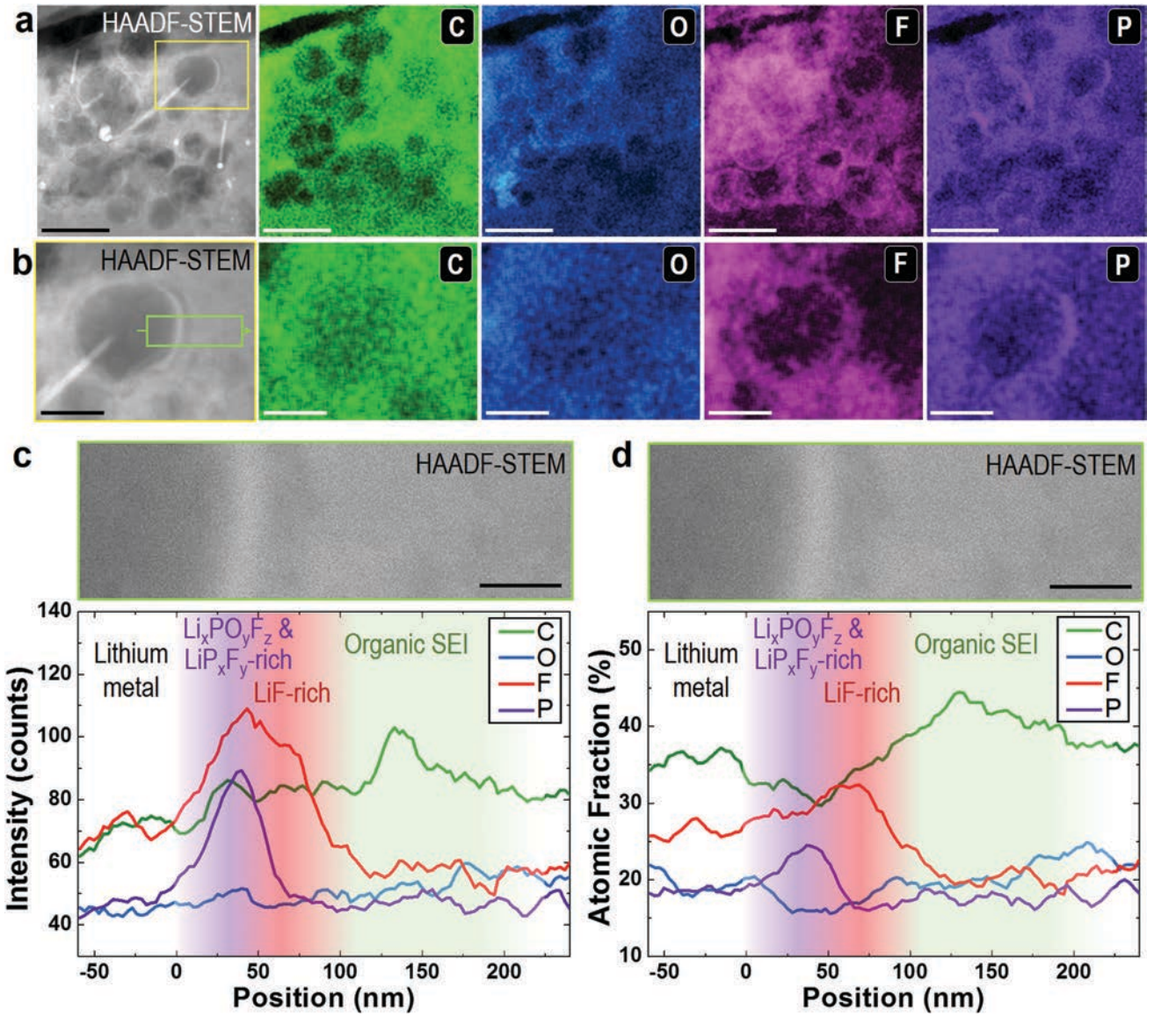

Fig. 4 Scanning TEM (STEM) energy-dispersive X-ray spectroscopy (EDS) analysis of the SEI on lithium nanogranules in the presence of the PDDA cationic polymer coating. (a) A high-angle annular dark-field (HAADF) STEM image and EDS elemental maps of lithium nanogranules and their SEI layers. Scale bars are 500 nm. (b) A magnified HAADF-STEM image and corresponding EDS elemental maps of a representative lithium nanogranule. The corresponding area is marked with a yellow box in the HAADF-STEM image in (a). Scale bars are 200 nm. (c and d) EDS line-scan profiles of the lithium nanogranule surface corresponding to the marked region in (b), where both the intensity (c) and atomic fraction (d) are obtained. Each point was integrated with a window of 100 pixels × 3 pixels (96.8 nm perpendicular and 2.9 nm parallel to the scanning line) to enhance the EDS signals. The corresponding HAADF-STEM image is shown above each profile for better understanding. Scale bars are 50 nm.

the liquid cell. Elemental maps of the titanium (Ti) electrode, tin (Sn) from the $Sn@SnO_2$ nanostructures, nitrogen (N) from the SiN membrane and PDDA, and chlorine (Cl) from the anion residue of PDDA are also obtained (Fig. S13, ESI†). An enlarged view of a region with a lithium nanogranule clearly shows the elemental distributions of C, O, F and P within the SEI layer and the electrolyte residue (Fig. 4b). It is notable that F is highly concentrated at the surface of the lithium nanogranule and uniformly distributed encircling the nanogranule. In contrast, P is concentrated only in certain regions around the lithium nanogranule. C and O are more broadly distributed both in the SEI layer and the surrounding electrolyte residue. The EDS quantifications show 41 at% F and 8 at% P in the whole area of Fig. 4a, among the total amount of C, O, F, and P (at% represents the atomic percent; see more in Table S2, ESI†). The F and P compositions in areas with only the electrolyte residue are significantly lower, *e.g.*, 4 at% F and 2 at% P (Fig. S14 and Table S3, ESI†). As a comparison, there are 7 at% F and 1 at% P, among the total amount of C, O, F, and P, in the fresh electrolyte (1 M $LiPF_6$ in PC). This suggests that fluorine and phosphorus are accumulated within the SEI layer during the growth of lithium nanogranules underneath the cationic polymer film.

EDS line-scan profiles across the SEI layer of a representative lithium nanogranule show more details of the elemental distribution within the SEI. The EDS line-scan profiles are collected from an area of 96.8 nm × 300 nm, as highlighted in Fig. 4b. Each point in the line-scan profile is integrated within a window of 100 pixels × 3 pixels (96.8 nm perpendicular and 2.9 nm parallel to the scanning line) to enhance the signals. Both intensity profiles and calculated atomic fraction profiles for each element (*i.e.*, C, O, F and P) are provided (Fig. 4c and d). We find that both the phosphorus and fluorine signals are the most intense near the lithium nanogranule surface. Phosphorus is concentrated in the 0–50 nm inner layer and fluorine is more broadly distributed in the 0–100 nm layer of the SEI. The distribution of phosphorus may vary in the 0–100 nm range depending on the lithium nanogranules. A slightly higher concentration of carbon and oxygen is found 100–200 nm above the nanogranule surface. This is consistent with the previous reports that SEIs consist of an inorganic inner layer (*e.g.*, LiF, LiP_xF_y, $Li_xPO_yF_z$, Li_2O, Li_2CO_3, *etc.*) and an organic outer layer.[39] Our EDS line-scan profiles reveal the spatial distributions of these compounds. For instance, LiF is 50–100 nm-thick within the inner layer. 50 nm-thick LiP_xF_y and $Li_xPO_yF_z$ reside within the inner layer of the SEI concentrated at some positions. We consider the uniform distribution of LiF within the inner layer of the SEI to be the key factor in the suppression of lithium dendrite growth; more will be discussed later. To the best of our knowledge, such a detailed chemical distribution within the SEI on individual lithium nanograins coupled with *in situ* experiments has not previously been achieved.

Lithium nanogranular growth in coin cell batteries

Lithium plating experiments are also performed using lithium battery coin cells to compare with the above *in situ* TEM experiments that used electrochemical nanobattery cells. Two types of Li/Cu coin cells are built, one with the PDDA cationic polymer film drop-casted on the Cu foil current collector and the other without the polymer film. The battery coin cells are discharged to a capacity of 1 mA h cm^{-2} (Fig. S15, ESI†). A high current density of 10 mA cm^{-2} is used to better match what was measured in the *in situ* liquid cell TEM experiments (Fig. 2). After the discharge, the coin cells are disassembled inside an Ar-filled glove box and the electrodes are transferred for scanning electron microscopy (SEM) imaging and XPS measurements.

The SEM images of the lithium plated on the Cu foil with and without the cationic polymer film show distinctly different morphologies (Fig. 5a and b). Without the polymer film, much larger lithium grains (in micrometers) can be found (Fig. 5a), while the lithium grown under the cationic polymer film shows a nanogranular morphology (Fig. 5b). These are consistent with our *in situ* liquid cell TEM experiment results (see more results in Fig. S16, ESI†).

The XPS spectra also show the influence of the cationic polymer film on lithium plating. Specifically, the surface chemistry of the plated lithium changes in the presence of the cationic polymer film coating on the electrode. XPS F 1s and P 2p spectra for the plated lithium with and without the cationic polymer film are shown in Fig. 5c. Additional spectra of C 1s, N 1s, O 1s, and Li 1s can be found in Fig. S17 (ESI†). The peak at ~686.7 eV in the F 1s spectra corresponds to LiP_xF_y/$Li_xPO_yF_z$, and the peak at ~684.8 eV is attributed to LiF.[40,41] It is clear that the concentration of LiF on the coated surface is significantly higher than that on the bare Cu foil. The P 2p spectra show that the concentration of another fluorinated lithium compound ($Li_xPO_yF_z$) also slightly increases in the polymer coated cell. These XPS results reflect the average distribution of different fluorinated compounds on the surface of the plated lithium (400 μm × 400 μm spot size). These results support our *in situ* TEM observations that fluorine and phosphorus accumulate under the cationic polymer film. The coin cell experimental results are further discussed in the ESI.†

It is worth noting that lithium nanogranular growth was also obtained on the cycled lithium metal anode in coin cells previously.[42] An electrolyte with a high concentration of fluorinated lithium salt (10 M lithium bis(fluorosulfonyl)imide (LiFSI) in ethylene carbonate/dimethyl carbonate (EC/DMC)) was used, which led to a high ratio of LiF on the lithium anode measured by XPS.[42]

Mechanisms of lithium dendrite suppression by a cationic polymer film

Our systematic *in situ* experimental results with complementary *ex situ* experiments reveal the mechanisms of lithium dendrite suppression by a cationic polymer film, which is not limited to PDDA. As shown in the schematic in Fig. 6, the cationic polymer can trap PF_6^- ions from the electrolyte through electrostatic attraction.[43,44] Thus, the electrode surface is surrounded by the electrolyte with abundant PF_6^- ions. As soon as lithium is deposited on the electrode surface through the reduction of Li^+ ions that permeated the polymer film, PF_6^- ions react with the lithium. It leads to the rapid formation of a 50–100 nm

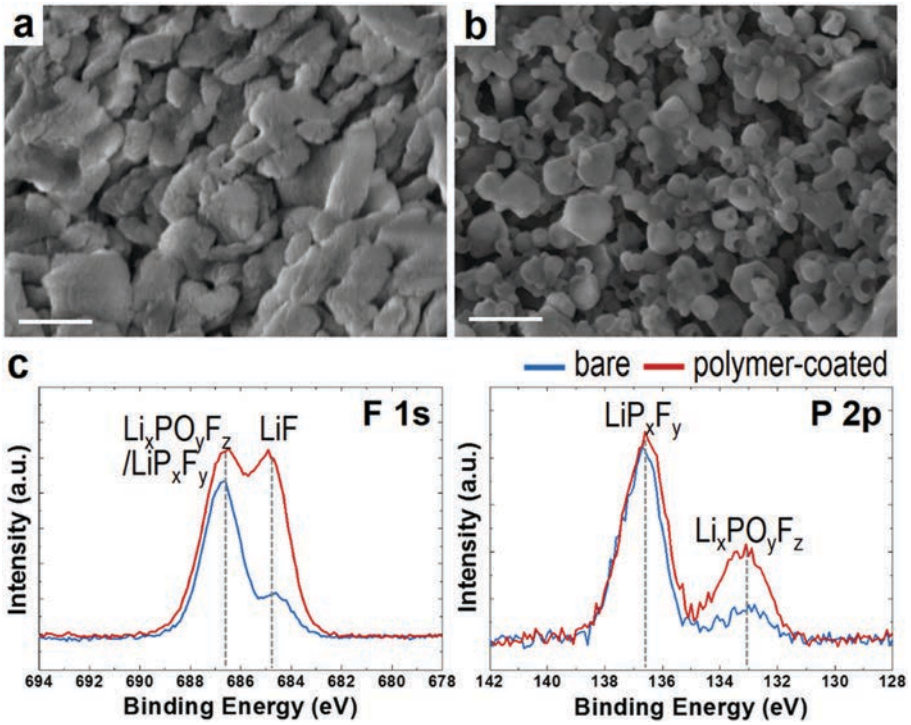

Fig. 5 Lithium metal electrochemically plated onto Cu foil in Li/Cu coin cells. A current density of 10 mA cm^{-2} and a capacity of 1 mA h cm^{-2} were used. (a and b) Scanning electron microscopy (SEM) images of electrochemically plated lithium (a) without and (b) with the cationic polymer coating on the Cu foil. Scale bars are 500 nm. (c) X-ray photoelectron spectroscopy (XPS) analysis of the plated lithium surface corresponding to the SEI. High-resolution XPS spectra of F 1s and P 2p peaks without (blue) and with (red) the cationic polymer film on the Cu foil.

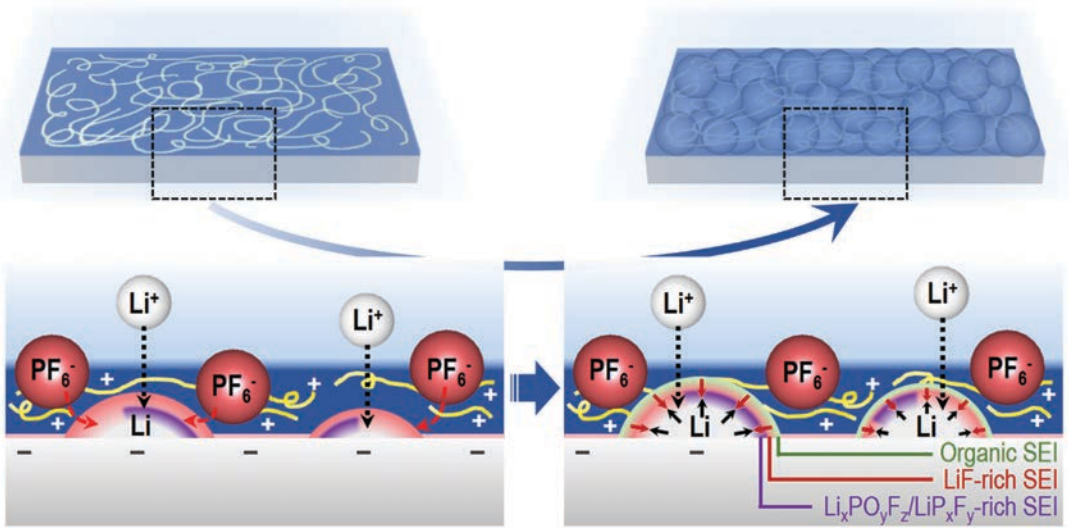

Fig. 6 A schematic drawing of the electrochemical growth mechanisms of lithium metal and the formation of the SEI with a cationic polymer film on the electrode.

thick LiF-rich SEI layer surrounding the lithium deposits. Fluorophosphates, such as LiP_xF_y, and $Li_xPO_yF_z$, can be also obtained almost at the same time. Possible chemical reactions are suggested in eqn (1)–(5)[45,46] below.

$$LiPF_6 + 2Li \rightarrow 3LiF + PF_3 \quad (1)$$

$$LiPF_6 \rightleftharpoons LiF + PF_5 \quad (2)$$

$$PF_5 + 2xLi \rightarrow xLiF + Li_xPF_{5-x} \quad (3)$$

$$PF_5 + H_2O \rightarrow POF_3 + 2HF \quad (4)$$

$$POF_3 + 2xLi \rightarrow xLiF + Li_xPOF_{3-x} \quad (5)$$

We consider that the instantaneous formation of a LiF-rich SEI on an individual lithium nanogranule suppresses its rapid

growth and promotes the nucleation of new lithium nanogranules. Thus, a layer of deposits with lithium nanogranules is achieved on the electrode during lithium plating. The formation of lithium nanogranules is not dependent on the specific electrode, since a similar morphology of lithium has been achieved on cycled lithium metal anodes[42,47] as well as on Cu electrodes (Fig. 5) in coin cells.

Although the lithium nanogranular growth arising from the LiF-rich SEI is consistent with the previous claims that LiF is effective in suppressing lithium dendritic growth,[10,42,47–51] the pathways of lithium dendrite suppression by the nanogranular growth of lithium have not been unveiled before. Previous studies were not able to elucidate the mechanisms of lithium nanogranular growth associated with the LiF-rich SEI,[42,47] which is largely due to the lack of ability to resolve the spatial distribution of SEI chemistry on individual lithium nanogranules and the dynamic lithium plating. Especially, it has not been possible to reveal the nanogranular growth of lithium induced by a cationic polymer film without high resolution *in situ* imaging technology.

This work provides additional insights into the LiF-rich SEI in controlling the growth of lithium. For instance, since the interfacial area is minimized in the nanogranular morphology of lithium, it implies the significance of high interfacial energy between Li and LiF for controlling the growth of lithium.[50] Moreover, since the sizes of Li nanogranules decrease with the increase of the cationic polymer density (higher PF_6^- anion concentration) (Fig. 3c), we postulate that a dense SEI or mechanically strong LiF-rich SEI (*i.e.* high bulk modulus[50]) may limit the Li-ion diffusion and reduce the growth of individual lithium nanogranules.

It is remarkable that a LiF-rich SEI on lithium nanogranules has been achieved in the conventional electrolyte without introducing extra fluorine sources (*e.g.* adding fluoroethylene carbonate (FEC) or LiF additives[10,48]). It demonstrates the great advantages of applying a cationic polymer film on the anode. The effectiveness of the PDDA cationic polymer film in lithium dendrite suppression is expected to be applicable to other systems. First, PF_6^- anions can be trapped by other cationic polymers due to electrostatic interactions. Second, since the PC solvent has a higher reduction potential than most other carbonates,[52,53] a LiF-rich SEI on lithium nanograins is also expected in other electrolytes. For example, PC may be replaced by various solvents, such as diethyl carbonate (DEC), dimethyl carbonate (DMC), ethyl methyl carbonate (EMC), *etc.* Considering the high reduction potential of the PF_6^- anion,[53] a LiF-rich SEI can be achieved with $LiPF_6$ salt in solvents other than carbonates as well. Other lithium salts containing fluorine, such as lithium bis(trifluoromethanesulfonimide) (LiTFSI), can also have similar effects given their high reduction potential.[53]

Lastly, our results show that several inorganic compounds, *e.g.*, fluorophosphates and fluorides, are distributed layer-by-layer within the SEI on individual lithium nanogranules (Fig. 4c and d). The different chemical/electrochemical reaction rates for each compound formation may have contributed to the layer-by-layer growth of different SEI compounds. The concentration variations of fluorophosphates within the SEI may have resulted from the self-agglomeration of the compound nanoparticles.[54] Unveiling of the layer-by-layer distribution of compounds within the SEI expands our knowledge of the SEI structure.[55]

Conclusions

In conclusion, this study demonstrates the unique capability of resolving the spatial distribution of SEI chemistry by *in situ* electrochemical liquid cell TEM. This capability allows us to uncover the mechanisms of lithium dendrite suppression by a cationic polymer film. We found that lithium nanogranules are formed when a PDDA cationic polymer film is applied on the electrode. This results from the cationic polymer film trapping of PF_6^- ions and thus the SEI chemistry on individual Li nanogranules being modified by forming a LiF-rich inner layer. The uniformly distributed LiF-rich SEI on individual lithium nanogranules assists the nucleation of new lithium nanogranules while suppressing the rapid growth of the existing nanogranules. Similar results are expected in other systems with different cationic polymers or electrolytes. This work sheds light on strategies for lithium dendrite suppression, for instance, a unique way to achieve a LiF-rich SEI without supplying extra fluorine in the electrolyte.

Experimental

Materials and synthesis

Poly(diallyldimethylammonium chloride) (PDDA) solution (20 wt% in H_2O, average M_w: 200 000–350 000), $SnCl_4$ (99.995%), $NaBH_4$ ($\geq$96%), 1 M lithium hexafluorophosphate in propylene carbonate (1 M $LiPF_6$ in PC) electrolyte, and lithium metal were purchased from Sigma Aldrich. The previously reported recipe was slightly modified for the synthesis of the Sn@SnO_2 nanostructure-assisted PDDA coating solution.[32] 0.5 mL PDDA and 0.1 g $NaBH_4$, a reducing agent, were dissolved in 60 ml deionized water. 0.09 g $SnCl_4$ solution diluted in 30 ml deionized water was added dropwise to the stirred PDDA + $NaBH_4$ solution. The synthesized gray solid products were washed with deionized water and ethanol lastly. The resulting products were dispersed in ethanol and thoroughly ultrasonicated to generate free-PDDAs, separated from the surface of Sn@SnO_2 nanostructures, for a better coating on the electrodes in the liquid TEM cells.

In situ liquid TEM experiments

Fabrication details of the electrode-deposited liquid cells for the *in situ* liquid cell TEM experiments are described in our earlier papers.[29,30] Titanium electrodes were deposited instead of the earlier gold electrodes considering the larger electrochemical stability window of titanium in lithium-based batteries.[56,57] UV-curing adhesives were used to seal the bottom/top chips after the TEM viewing-window alignment, which are chemically stable with the liquid electrolyte and firmly cured within 30 seconds of UV-light exposure. The synthesized Sn@SnO_2

nanostructure-assisted PDDA coating solution was loaded through the reservoir of the assembled electrochemical liquid TEM cell and dried overnight for the investigation of lithium growth under the cationic polymer film. The solution flows through the gap between the top and bottom chips by capillary force. Lithium flakes were attached onto both Ti electrodes exposed in the reservoirs of the assembled chips to construct the Li/Li symmetric cell. The liquid electrolyte (1 M $LiPF_6$ in PC) was loaded through the reservoirs by a pipette and the reservoirs were sealed by the UV-curing adhesive. Electrically conducting wires connected to the Ti electrodes and protruding from the liquid TEM cell were pasted onto the cables at the tip of the customized TEM holder by a silver conductive paint. The cables from the other side of the TEM holder were connected to a potentiostat (CH Instruments). For the *in situ* TEM-voltammetry measurements, a linear sweep potential was applied to the electrode up to ±4–6 V at a 0.1 V s^{-1} sweep rate, considering the higher resistance of the electrode-deposited liquid TEM cells than the typical coin-type battery cells, and the ending potential was constantly applied to continue the reaction. Voltage and current profiles are shown in Fig. S11 and further discussed in the ESI.† An electron beam with a very low electron dose rate of ~0.2–0.5 e^- $Å^{-2}$ s^{-1} was used during the *in situ* TEM experiments to avoid unexpected electron beam-induced reactions. The *in situ* TEM lithium plating reactions were recorded at two frames per second using a charge-coupled device (CCD) installed in the TEM. For the STEM-EDS analysis, a low but slightly higher dose rate TEM electron beam (~1 e^- $Å^{-2}$ s^{-1}) was used to steadily irradiate the liquid electrolyte for more than 20 minutes to make a protection layer on the *in situ* grown lithium by the e-beam polymerization of the liquid electrolyte.[58] Then, the liquid TEM cell was carefully separated to perform the STEM-EDS experiments in order to achieve enhanced EDS signals. The top and bottom SiN membranes remained on both sides of the *in situ* grown lithium after the cell separation, making double protection layers with the polymerized electrolyte. The *in situ* liquid TEM experiment was performed with a JEOL JEM-2100 200 kV LaB_6 TEM instrument and the following STEM-EDS experiment was performed with an FEI ThemIS 300 kV field-emission TEM instrument equipped with Bruker SuperX EDS detectors.

Lithium plating in coin-type cells and characterization

Half inch copper foil was washed with 1.0 M hydrochloric acid solution for 10 minutes, then rinsed with water (3 times), followed by an ethanol wash (3 times), and dried under a vacuum for 12 hours at room temperature. To construct the Li/Cu coin cell with the cationic polymer film, approximately 50 μl of 2 wt% PDDA in ethanol solution was drop-cast onto the copper foil and dried under a vacuum for 3 days at room temperature. CR2032 coin-type cells were assembled with the PDDA coated copper foil (or bare copper foil as a control experiment), lithium foil, a Celgard 3501 separator, and 1 M $LiPF_6$ in PC electrolyte in an Ar-filled glove box (less than 0.1 ppm of O_2 and 0.0 ppm of H_2O). Electrochemical tests were performed using a battery cycler (VMP3; Bio-Logic Science Instruments). The cells were discharged at a 10 mA cm^{-2} current density to a capacity of 1 mA h cm^{-2}. For SEM and XPS experiments of the lithium plated onto the copper foil, the discharged cells were opened in the Ar-filled glove box and the lithium-plated copper foil was washed with dimethyl carbonate solvent to remove $LiPF_6$ residue. For the SEM experiment, the sample was transferred in an air-sealing bag to the SEM room to minimize the air-exposure. SEM images of the lithium on the copper foil were acquired at an acceleration voltage of 3 kV (Gemini Supra 55-VP; Zeiss). For the XPS experiment, the samples were loaded onto the transfer holder in the glove box and the transfer holder was pumped down to ensure the samples were not exposed to air. XPS spectra were obtained with an Al K-alpha X-ray source, 400 μm × 400 μm spot size, 0.1 eV step size, and 50 ms dwell time (K-Alpha Plus; Thermo Scientific).

Conflicts of interest

There are no conflicts to declare.

Acknowledgements

This work was supported by the U.S. Department of Energy (DOE), Office of Science, Office of Basic Energy Sciences (BES), Materials Sciences and Engineering Division under Contract No. DE-AC02-05-CH11231 within the KC22ZH program. Work at the Molecular Foundry of Lawrence Berkeley National Laboratory (LBNL) was supported by the Office of Science, Office of Basic Energy Sciences, of the U.S. Department of Energy under Contract No. DE-AC02-05CH11231. STEM-EDS experiments were conducted using the ThemIS TEM instrument at National Center for Electron Microscopy (NCEM) of LBNL. S. Y. L. was supported by a LDRD fund at LBNL. S. J. H. was supported by the Assistant Secretary for Energy Efficiency, Vehicle Technologies Office of the US Department of Energy under the Advanced Battery Materials Research Program. We thank Dr Yu Wang, Dr Karen Bustillo, Dr Rohan Dhall, Dr Chengyu Song, Dr Stefano Cabrini, and Dr Selven Virasawmy at LBNL for useful discussions and their generous help in setting up the experiments.

References

1 D. C. Lin, Y. Y. Liu and Y. Cui, *Nat. Nanotechnol.*, 2017, **12**, 194–206.
2 J. Lopez, D. G. Mackanic, Y. Cui and Z. N. Bao, *Nat. Rev. Mater.*, 2019, **4**, 312–330.
3 Y. Y. Liu, D. C. Lin, P. Y. Yuen, K. Liu, J. Xie, R. H. Dauskardt and Y. Cui, *Adv. Mater.*, 2017, **29**, 1605531.
4 K. Liu, A. Pei, H. R. Lee, B. Kong, N. Liu, D. C. Lin, Y. Y. Liu, C. Liu, P. C. Hsu, Z. A. Bao and Y. Cui, *J. Am. Chem. Soc.*, 2017, **139**, 4815–4820.
5 R. Xu, X. Q. Zhang, X. B. Cheng, H. J. Peng, C. Z. Zhao, C. Yan and J. Q. Huang, *Adv. Funct. Mater.*, 2018, **28**, 1705838.

6 Y. Gao, Z. F. Yan, J. L. Gray, X. He, D. W. Wang, T. H. Chen, Q. Q. Huang, Y. G. C. Li, H. Y. Wang, S. H. Kim, T. E. Mallouk and D. H. Wang, *Nat. Mater.*, 2019, **18**, 384–389.
7 Y. P. Sun, Y. Zhao, J. W. Wang, J. N. Liang, C. H. Wang, Q. Sun, X. T. Lin, K. R. Adair, J. Luo, D. W. Wang, R. Y. Li, M. Cai, T. K. Sham and X. L. Sun, *Adv. Mater.*, 2019, **31**, 1806541.
8 J. Luo, C. C. Fang and N. L. Wu, *Adv. Energy Mater.*, 2018, **8**, 1701482.
9 X. B. Cheng, R. Zhang, C. Z. Zhao, F. Wei, J. G. Zhang and Q. Zhang, *Adv. Sci.*, 2016, **3**, 1500213.
10 X. Q. Zhang, X. B. Cheng, X. Chen, C. Yan and Q. Zhang, *Adv. Funct. Mater.*, 2017, **27**, 1605989.
11 E. Markevich, G. Salitra, F. Chesneau, M. Schmidt and D. Aurbach, *ACS Energy Lett.*, 2017, **2**, 1321–1326.
12 D. Ostrovskii, F. Ronci, B. Scrosati and P. Jacobsson, *J. Power Sources*, 2001, **94**, 183–188.
13 Y. Z. Li, Y. B. Li, A. L. Pei, K. Yan, Y. M. Sun, C. L. Wu, L. M. Joubert, R. Chin, A. L. Koh, Y. Yu, J. Perrino, B. Butz, S. Chu and Y. Cui, *Science*, 2017, **358**, 506–510.
14 M. J. Zachman, Z. Y. Tu, S. Choudhury, L. A. Archer and L. F. Kourkoutis, *Nature*, 2018, **560**, 345–349.
15 Y. Zhou, M. Su, X. Yu, Y. Zhang, J.-G. Wang, X. Ren, R. Cao, W. Xu, D. R. Baer, Y. Du, O. Borodin, Y. Wang, X.-L. Wang, K. Xu, Z. Xu, C. Wang and Z. Zhu, *Nat. Nanotechnol.*, 2020, **15**, 224–230.
16 A. L. Pont, R. Marcilla, I. De Meatza, H. Grande and D. Mecerreyes, *J. Power Sources*, 2009, **188**, 558–563.
17 G. B. Appetecchi, G. T. Kim, M. Montanina, M. Carewska, R. Marcilla, D. Mecerreyes and I. De Meatza, *J. Power Sources*, 2010, **195**, 3668–3675.
18 G. G. Eshetu, D. Mecerreyes, M. Forsyth, H. Zhang and M. Armand, *Mol. Syst. Des. Eng.*, 2019, **4**, 294–309.
19 L. J. Li, L. Ma and B. A. Helms, *Macromolecules*, 2018, **51**, 7666–7671.
20 L. J. Li, T. A. Pascal, J. G. Connell, F. Y. Fan, S. M. Meckler, L. Ma, Y. M. Chiang, D. Prendergast and B. A. Helms, *Nat. Commun.*, 2017, **8**, 2277.
21 H. P. Su, C. Y. Fu, Y. F. Zhao, D. H. Long, L. C. Ling, B. M. Wong, J. Lu and J. C. Guo, *ACS Energy Lett.*, 2017, **2**, 2591–2597.
22 X. S. Zhou, Y. X. Yin, L. J. Wan and Y. G. Guo, *Adv. Energy Mater.*, 2012, **2**, 1086–1090.
23 X. H. Xiong, C. H. Yang, G. H. Wang, Y. W. Lin, X. Ou, J. H. Wang, B. T. Zhao, M. L. Liu, Z. Lin and K. Huang, *Energy Environ. Sci.*, 2017, **10**, 1757–1763.
24 N. P. Liang, J. H. Fang and X. X. Guo, *J. Mater. Chem. A*, 2017, **5**, 15087–15095.
25 X. W. Li, Z. X. Zhang, S. J. Li, L. Yang and S. Hirano, *J. Power Sources*, 2016, **307**, 678–683.
26 S. Kalnaus, Y. L. Wang and J. A. Turner, *J. Power Sources*, 2017, **348**, 255–263.
27 C. T. Love, *J. Power Sources*, 2011, **196**, 2905–2912.
28 Y. J. Yang, X. Z. Liu, Z. H. Dai, F. L. Yuan, Y. Bando, D. Golberg and X. Wang, *Adv. Mater.*, 2017, **29**, 1606922.
29 Z. Y. Zeng, W. I. Liang, H. G. Liao, H. L. L. Xin, Y. H. Chu and H. M. Zheng, *Nano Lett.*, 2014, **14**, 1745–1750.
30 M. H. Sun, H. G. Liao, K. Y. Niu and H. M. Zheng, *Sci. Rep.*, 2013, **3**, 3227.
31 Y. Iamphaojeen and P. Siriphannon, *Int. J. Polym. Mater. Polym. Biomater.*, 2014, **63**, 918–922.
32 N. Du, H. Zhang, B. Chen, X. Ma and D. Yang, *Chem. Commun.*, 2008, 3028–3030.
33 S. Y. Lee, K. Y. Park, W. S. Kim, S. Yoon, S. H. Hong, K. Kang and M. Kim, *Nano Energy*, 2016, **19**, 234–245.
34 Z. Y. Zeng, X. W. Zhang, K. Bustillo, K. Y. Niu, C. Gammer, J. Xu and H. M. Zheng, *Nano Lett.*, 2015, **15**, 5214–5220.
35 M. Gu, L. R. Parent, B. L. Mehdi, R. R. Unocic, M. T. McDowell, R. L. Sacci, W. Xu, J. G. Connell, P. H. Xu, P. Abellan, X. L. Chen, Y. H. Zhang, D. E. Perea, J. E. Evans, L. J. Lauhon, J. G. Zhang, J. Liu, N. D. Browning, Y. Cui, I. Arslan and C. M. Wang, *Nano Lett.*, 2013, **13**, 6106–6112.
36 P. Bai, J. Li, F. R. Brushett and M. Z. Bazant, *Energy Environ. Sci.*, 2016, **9**, 3221–3229.
37 A. Kushima, K. P. So, C. Su, P. Bai, N. Kuriyama, T. Maebashi, Y. Fujiwara, M. Z. Bazant and J. Li, *Nano Energy*, 2017, **32**, 271–279.
38 K. N. Wood, M. Noked and N. P. Dasgupta, *ACS Energy Lett.*, 2017, **2**, 664–672.
39 E. Peled and S. Menkin, *J. Electrochem. Soc.*, 2017, **164**, A1703–A1719.
40 S. J. Lee, J. G. Han, Y. Lee, M. H. Jeong, W. C. Shin, M. Ue and N. S. Choi, *Electrochim. Acta*, 2014, **137**, 1–8.
41 P. C. Shi, H. Zheng, X. Liang, Y. Sun, S. Cheng, C. H. Chen and H. F. Xiang, *Chem. Commun.*, 2018, **54**, 4453–4456.
42 X. L. Fan, L. Chen, X. Ji, T. Deng, S. Y. Hou, J. Chen, J. Zheng, F. Wang, J. J. Jiang, K. Xu and C. S. Wang, *Chem*, 2018, **4**, 174–185.
43 G. S. Manning, *Acc. Chem. Res.*, 1979, **12**, 443–449.
44 T. Alfrey, P. W. Berg and H. Morawetz, *J. Polym. Sci.*, 1951, **7**, 543–547.
45 D. Aurbach, B. Markovsky, A. Shechter, Y. EinEli and H. Cohen, *J. Electrochem. Soc.*, 1996, **143**, 3809–3820.
46 C. G. Barlow, *Electrochem. Solid-State Lett.*, 1999, **2**, 362–364.
47 S. Choudhury and L. A. Archer, *Adv. Electron. Mater.*, 2016, **2**, 1500246.
48 Y. Y. Lu, Z. Y. Tu and L. A. Archer, *Nat. Mater.*, 2014, **13**, 961–969.
49 D. C. Lin, Y. Y. Liu, W. Chen, G. M. Zhou, K. Liu, B. Dunn and Y. Cui, *Nano Lett.*, 2017, **17**, 3731–3737.
50 X. L. Fan, X. Ji, F. D. Han, J. Yue, J. Chen, L. Chen, T. Deng, J. J. Jiang and C. S. Wang, *Sci. Adv.*, 2018, **4**, eaau9245.
51 L. M. Suo, W. J. Xue, M. Gobet, S. G. Greenbaum, C. Wang, Y. M. Chen, W. L. Yang, Y. X. Li and J. Li, *Proc. Natl. Acad. Sci. U. S. A.*, 2018, **115**, 1156–1161.
52 A. P. Wang, S. Kadam, H. Li, S. Q. Shi and Y. Qi, *npj Comput. Mater.*, 2018, **4**, 15.

53 S. A. Delp, O. Borodin, M. Olguin, C. G. Eisner, J. L. Allen and T. R. Jow, *Electrochim. Acta*, 2016, **209**, 498–510.
54 X. X. Cai, B. P. Li, Y. Pan and G. Z. Wu, *Polymer*, 2012, **53**, 259–266.
55 E. Peled, D. Golodnitsky and G. Ardel, *J. Electrochem. Soc.*, 1997, **144**, L208–L210.
56 S. T. Myung, Y. Sasaki, S. Sakurada, Y. K. Sun and H. Yashiro, *Electrochim. Acta*, 2009, **55**, 288–297.
57 C. W. Bale, *Bull. Alloy Phase Diagrams*, 1989, **10**, 135–138.
58 I. A. Shkrob, Y. Zhu, T. W. Marin and D. Abraham, *J. Phys. Chem. C*, 2013, **117**, 19270–19279.